Model-Based Estimation of Lithium Concentrations and Temperature in Batteries Using Soft-Constrained Dual Unscented Kalman Filtering

Stefano Marelli and Matteo Corno

***Abstract*— This brief proposes an electrochemical model-based estimator of the Lithium-ion (Li-ion) concentration and temperature of a Li-ion cell. The use of the electrochemical approach allows for the estimation of the spatial distribution of lithium concentration and temperature. The estimation is based on a soft-constrained dual unscented Kalman filter (DUKF) designed on the pseudo-2-D model of a Li-ion cell. The dual structure, along with parallelization, reduces the computational complexity, whereas the soft-constraint improves convergence. A simulation analysis validates the approach showing bulk state of charge (SoC) estimation error lower than 1.5%, solid-phase lithium concentration estimation errors of less than 4%, and temperature estimation errors within 0.2 °C from the true value in any point of the cell.**

***Index Terms*— Dual unscented Kalman filter, electrochemical–thermal model, Li-ion batteries, soft-constraint.**

I. Introduction

LITHIUM-ION (Li-ion) batteries are the most widely adopted technology for electric mobility and consumer electronics. Li-ion batteries require battery management systems (BMSs) to be safely operated [1], [2]. The BMS prevents internal states from exceeding safe limits. In demanding current conditions, while averaged electrochemical quantities such as voltage (V) and state of charge (SoC) may reside in their safe region, areas in the electrodes may suffer from local conditions that are detrimental to the cell life and/or performance [3]. For this reason, using reactions overpotentials and lithium concentration limitations rather than voltage limitations leads to improvements in terms of energy extraction and aging. This approach can only be implemented if a sufficiently accurate estimate of the lithium concentrations available [4]. In addition, electrochemical dynamics are heavily affected by temperature [5] and large differences between surface and core temperatures can occur during normal cell operation [6]. Similar to what happens for concentrations, if one only monitors the average temperature, a thermal runaway may not be promptly detected, thus leading to premature cell degradation [7].

Several models of Li-ion batteries exist. They are classified according to their complexity and accuracy from very simple electro-equivalent models to fully computational fluid dynamics (CFDs) models. The choice of the model entails different estimation accuracy. In [8], the authors employ a simple electro-equivalent model to estimate average quantities. The single particle model (SPM) is a rather common and successful approach that accounts for the electrochemical dynamics in a simplified fashion and yields good results in estimation [9]. For example, in [10], the authors adopt an approximated version of the SPM and propose a way to compensate for model uncertainty and electrolyte dynamics simplification. The pseudo-2-dimensional (P2D) electrochemical model, adopted in works such as [11]–[15], is widely recognized as a valuable tradeoff between detailed modeling and computational cost. This model, relying on partial differential algebraic equations (PDAEs), requires particular care in the implementation and in the observer formulation.

In this brief, the P2D model is coupled with a distributed thermal model of a cylindrical Li-ion cell. A finite difference method (FDM) space-discretization technique is employed for the PDAEs, because it allows for easy order rescaling while maintaining the physical meaning of all the variables and parameters. Elsewhere, the P2D model is employed by proposing different approaches for order reduction: Smith *et al.* [4] estimate the instantaneous available current; in a previous contribution, we estimate the bulk SoC using an extended Kalman filter (EKF) on a space-discretized and reduced-order version of the P2D model [16]; Finally, Bizeray *et al.* [15] estimate the lithium concentrations and a bulk temperature using orthogonal collocation and a Kalman filter.

To the best of the authors' knowledge, the field of simultaneous spatially distributed concentration and temperature estimation is still rather unexplored. This brief extends our previous contribution [17], where we estimate only the lithium concentrations disregarding the temperature. In this brief, we propose an approach to estimate both the electrochemical and thermal states. The algorithm estimates both the average values of these states as well as their spatial distribution. This information is critical to achieve full exploitation of a cell, minimizing the risk of damaging it. We achieve our objective using a soft-constrained dual unscented Kalman filter (DUKF). In summary, in this brief, we propose an estimator capable of

1) synchronously estimating local lithium concentration and temperature inside the cell;
2) improving convergence, thanks to a physically motivated soft-constrained approach that promotes the conservation of mass;

Manuscript received May 22, 2019; revised November 25, 2019 and February 3, 2020; accepted February 9, 2020. Date of publication April 7, 2020; date of current version February 9, 2021. Manuscript received in final form February 10, 2020. This work was financial supported by the Ministero dell'Istruzione, dell'Università e della Ricerca Scientific Independence of young Researchers (SIR) under Project RBSI14STHV. Recommended by Associate Editor C. Manzie. *(Corresponding author: Matteo Corno.)*

The authors are with the Dipartimento di Elettronica, Informazione e Bioingegneria at Politecnico di Milano, 20133 Milan, Italy (e-mail: stefano.marelli@polimi.it; matteo.corno@polimi.it).

Color versions of one or more of the figures in this article are available online at https://ieeexplore.ieee.org.

Digital Object Identifier 10.1109/TCST.2020.2974176

3) improving computational efficiency thanks to parallelization. The algorithm does not require a parallel implementation, but, as automotive-grade multicore hardware is becoming more common [18], our implementation is capable of exploiting its advantages.

The estimation is based on a DUKF, this design is advantageous under several aspects:

1) It does not require a closed-form of the dynamic system, thus avoiding the need to solve the algebraic constraints analytically or to numerically compute the Jacobian. An EKF implementation would require either operation.
2) The UKF is more computationally efficient (having fewer particles) than particle filters.
3) It can easily accommodate the inclusion of soft-constraints that, this brief shows, improve estimation convergence.
4) It is prone to parallel implementation.
5) The dual structure allows for a reduction of the order of the model used in the estimation without appreciable loss of accuracy.

Note that the proposed approach neglects aging phenomena. While extremely important, aging phenomena dynamics are slower than thermal and diffusion dynamics. Another observer could be designed to estimate aging and update the model parameters as [19] does for the SPM.

This brief is structured as follows. Section II briefly recalls the coupled electrochemical–thermal model. Section III details the soft-constrained DUKF. Section IV validates the approach through a simulation campaign before the final conclusions are drawn in Section V.

II. Coupled Electrochemical–Thermal Model

This section recalls the model used in designing the observer. The model is composed of two parts, namely the P2D electrochemical model and the thermal model. The P2D model describes the dynamics of the concentrations of lithium in the cell; the thermal model describes the temperature dynamics, driven by local heat generation mechanisms. These two parts exhibit bidirectional interactions, in that the electrochemical reactions influence the temperature dynamics and vice versa.

A. P2D Electrochemical Model

The P2D is a standard and accepted model in control-oriented electrochemical modeling of Li-ion cells. It describes the dual-intercalation process along one physical dimension (the cell longitudinal axis) and a pseudo-dimension (the radius of the active particles). In the model, c_s is the lithium concentration in solid phase; c_e is the Li-ion concentration in electrolyte phase; i_s is the electronic current in solid phase; i_e is the ionic current in electrolyte phase; ϕ_s is the solid-phase potential; ϕ_e is the electrolyte-phase potential, j^{Li} is the molar flux, η is the reaction overpotential. I is the cell current, which is the input of this model (assumed positive in discharge). Also, D_s is the solid-phase diffusion coefficient; F is Faraday's constant; a_s is the electrode specific interfacial area; D_e^{eff} is the effective diffusion coefficient; t_+^0 is Li-ion transference number (assumed as a constant); σ^{eff} is the effective conductivity; k^{eff} is the effective ionic conductivity, while k_D^{eff} is the effective diffusion conductivity. Finally, a few geometrical quantities are defined: A is the electrode plate area; δ_n, δ_p, and δ_s are the negative and positive electrodes and separator thicknesses; $L = \delta_n + \delta_p + \delta_s$ is the overall film thickness; R_s is the radius of the active material spherical particles.

We employ the FDM to spatially discretize the P2D model: the cell is discretized along x in N_n, N_p, and N_s elements, respectively, for the negative and positive electrodes, and the separator; each element occupies a space Δx_n, Δx_p, and Δx_s. Each electrode is modeled as a collection of active material spherical particles equal to the ratio between the effective electrode volume and the volume of a single sphere

$$\nu_n = \frac{\delta_n \ A \ \varepsilon_{s;n}}{\frac{4}{3}\pi R_s^3}; \quad \nu_p = \frac{\delta_p \ A \ \varepsilon_{s;p}}{\frac{4}{3}\pi R_s^3}$$

where $\varepsilon_{s;n}$ is the solid-phase volume fraction of negative electrode and $\varepsilon_{s;p}$ of the positive electrode. As such, in each discretized element of the electrodes, there is a number of spherical particles respectively equal to

$$\nu_n^{\Delta x} = \frac{\nu_n}{N_n}; \quad \nu_p^{\Delta x} = \frac{\nu_p}{N_p}.$$

Each active material spherical particle is further discretized along its radius r in N_r elements, spaced with Δr. Since all equations are written with volume-specific quantities, there is no need to consider all the $\nu_n^{\Delta x}$ and $\nu_p^{\Delta x}$ spheres for each discretized element, but just one sphere is representative also for the dynamics of all the others within the same element. Overall, the electrochemical model is described by $(N_r+1)(N_n+N_p)+N_s$ ordinary differential equations (ODEs), plus $5(N_n + N_p) + 2N_s - 3$ nonlinear algebraic constraints.

The conservation equations for the resulting discretized model are summarized in Table I, in the form of differential algebraic equations (DAEs). In the table and in the following, index m identifies discretized elements along x and index p along r. The discretized Butler–Volmer kinetics equation results

$$j_m^{\mathrm{Li}} = a_s j_0 \left[\exp\left(\frac{\alpha_a F}{RT}\eta_m\right) - \exp\left(-\frac{\alpha_c F}{RT}\eta_m\right)\right] \tag{1}$$

where α_a and α_c are the anodic and cathodic transfer coefficients, respectively; R is the universal gas constant; T is the temperature at which the reaction takes place; j_0 is the exchange current density. The reaction overpotential is defined as

$$\eta_m = \phi_{s,m} - \phi_{e,m} - U(c_{s,(m,N_r)})$$

where U is the thermodynamic equilibrium potential and is a nonlinear function of the surface concentration c_{se} [12]. Furthermore, we can write

$$i_{s,m} - i_{s,m-1} = -\Delta x_m j_m^{\mathrm{Li}}, \quad i_{e,m} - i_{e,m-1} = \Delta x_m j_m^{\mathrm{Li}}.$$

The cell output equation is

$$V = \phi_{s,N_n+N_s+N_p} - \phi_{s,1} - \frac{R_f}{A} I$$

TABLE I
DISCRETIZED ELECTROCHEMICAL MODEL—CONSERVATION DAES (BOUNDARY CONDITIONS ARE MARKED WITH GRAY BACKGROUND)

Species: solid phase
$\dot{c}_{s,(m,p)} = \frac{D_s}{(p\Delta r)^2}\left[2p\Delta r\left(\frac{c_{s,(m,p+1)} - c_{s,(m,p)}}{\Delta r}\right) + (p\Delta r)^2\left(\frac{c_{s,(m,p-1)} - 2c_{s,(m,p)} + c_{s,(m,p+1)}}{\Delta r^2}\right)\right]$
$c_{s,(m,1)} - c_{s,(m,0)} = 0$
$D_s\left(\frac{c_{s,(m,N_r+1)} - c_{s,(m,N_r)}}{\Delta r}\right) = \frac{-j_m^{Li}}{a_s F}$
Species: electrolyte phase
$\dot{c}_{e,m} = \frac{D_e^{eff}}{\varepsilon_e}\left(\frac{c_{e,m-1} - 2c_{e,m} + c_{e,m+1}}{\Delta x_m^2}\right) + \frac{1 - t_+^0}{F\varepsilon_e} j_m^{Li}$
$c_{e,1} - c_{e,0} = 0$
$c_{e,N_n+N_s+N_p+1} - c_{e,N_n+N_s+N_p} = 0$
Charge: solid phase
$i_{s,m} = -\sigma^{eff}\left(\frac{\phi_{s,m+1} - \phi_{s,m}}{\Delta x_m}\right)$
$i_{s,N_n} = i_{s,N_n+N_s} = 0$
$i_{s,0} = i_{s,N_n+N_s+N_p} = \frac{I}{A}$
Charge: Electrolyte Phase
$i_{e,m} = -k^{eff}\left(\frac{\phi_{e,m+1} - \phi_{e,m}}{\Delta x_m}\right) - k_D^{eff}\left(\frac{ln(c_{e,m+1}) - ln(c_{e,m})}{\Delta x_m}\right)$
$\phi_{e,1} - \phi_{e,0} = 0$
$\phi_{e,N_n+N_s+N_p+1} - \phi_{e,N_n+N_s+N_p} = 0$

where R_f is the electrode surface film resistance. Finally, the SoC is computed as

$$\text{SoC} = \frac{1}{N_n R_s^3}\sum_{m=1}^{N_n}\sum_{p=1}^{N_r} c_{s,(m,p)}\left(r_p^3 - r_{p-1}^3\right) \tag{2}$$

where r_p is the radius of the pth discretized element, equal to $p\Delta r$.

The coupling with the thermal part of the model takes place through the temperature term T. It determines the values of the exchange current density i_0, the diffusion coefficient in the solid phase D_s, the diffusion coefficient in the electrolyte phase D_e, and the electrolyte ionic conductivity k. All these parameters depend on the temperature according to the Arrhenius equation (see [20])

$$\Psi(T) = \Psi_{\text{act}}\exp\left[\frac{E_{\text{act}}^{\Psi}}{R}\left(\frac{1}{T_{\text{act}}} - \frac{1}{T}\right)\right] \tag{3}$$

where Ψ is the generic parameter, Ψ_{act} is the value of the parameter at the reference temperature $T_{\text{act}} = 25\,^{\circ}\text{C}$, E_{act}^{Ψ} is the activation energy for the parameter Ψ. Note that the dependence on the temperature effectively introduces a spatial dependence of the cited parameters. To better understand this dependence, we introduce the thermal model.

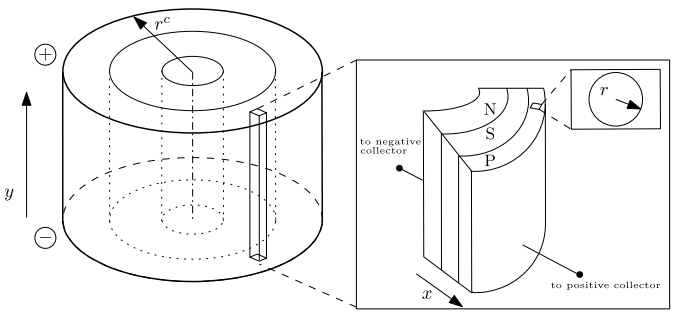

Fig. 1. Discretization of Li-ion cell along the r^c direction.

B. Thermal Model

The thermal model describes the heat generation mechanisms by means of partial differential equations (PDEs). It assumes that the temperature gradient along the cylinder *axial direction* y is negligible (see [21], [22]); thus, the temperature dynamics are those of heat conduction along the radius of a cylinder.

Also in this case, the model PDEs are discretized using the FDM, as depicted in Fig. 1. The cell is discretized along r^c in N_c elements, using a constant-volume approach. This means that all the N_c subcells have the same volume, and the resulting radial increment is not uniform.

The temperature dynamics are

$$\rho c_p \dot{T}_z = k_t\left[\frac{T_{z-1} - 2T_z + T_{z+1}}{\left(\Delta r_z^c\right)^2}\right] + \frac{k_t}{r_z^c}\left[\frac{T_{z+1} - T_z}{\Delta r_z^c}\right] + Q_z$$

which is a set of N_c ODEs with boundary conditions

$$T_1 - T_0 = 0, \quad \frac{T_{N_c+1} - T_{N_c}}{\Delta r_{N_c}^c} = -\frac{h}{k_t}(T_{N_c} - T_\infty).$$

In the equations above, index z is used for discretized elements along r^c. The radial increment Δr_z^c is the space occupied by the zth subcell

$$\Delta r_z^c = r_z^c - r_{z-1}^c.$$

T_∞ is the environment temperature (considered constant), k_t is the thermal conductivity, ρ is the density, h is the convection heat transfer coefficient, c_p is the specific heat capacity, Q is the volumetric heat generation rate, and R^c is the radius of the cylinder. Since the cylinder is a heterogeneous domain, being composed of two different phases (solid and electrolyte) distributed in three domains (negative electrode, positive electrode, and separator), the heat capacity C_p with the method proposed in [23] and using the parameters of the cell under study

$$C_p = \rho c_p = \sum_{i,k}\frac{\delta_i \varepsilon_{k,i}\rho_{k,i}c_{p,k,i}}{L}$$

where subscript $k = (s, e)$ indicates the phase (solid or electrolyte) and subscript $i = (n, s, p)$ indicates the component.

The volumetric heat generation is

$$Q_z = Q_{j,z} + Q_{o,z} + Q_{f,z}$$

and

$$Q_{j,z} = \frac{1}{L}\sum_m j^{\mathrm{Li}}_{m,z}\eta_{m,z}\Delta x_m$$

$$Q_{o,z} = \frac{1}{L}\sum_m \Bigg[\sigma^{\mathrm{eff}}\left(\frac{\phi_{s,m+1,z}-\phi_{s,m,z}}{\Delta x_m}\right)^2 + k^{\mathrm{eff}}\left(\frac{\phi_{e,m+1,z}-\phi_{e,m,z}}{\Delta x_m}\right)^2 + k_D^{\mathrm{eff}}\left(\frac{\ln(c_{e,m+1,z})-\ln(c_{e,m,z})}{\Delta x_m}\right)\cdot\left(\frac{\phi_{e,m+1,z}-\phi_{e,m,z}}{\Delta x_m}\right)\Bigg]\Delta x_m$$

$$Q_{f,z} = \frac{R_f}{L}\left(\frac{I_z}{A_z}\right)^2.$$

The term I_z is the input current to the zth subcell (a fraction of the total input current I), while A_z is the subcell electrode plate area.

The entire volume of the cell is divided into N_c subcells, each characterized by its own temperature, and consequently by a set of time-varying parameters to be used in the electrochemical model as discussed in (3). This yields a total of $N_c[(N_r+1)(N_n+N_p)+N_s]$ states for the discretized coupled electrochemical–thermal model. Also, since the current collector is a common element of all subcells, they are all connected in parallel; this means that they exhibit the same terminal voltage. Thus, an additional set of algebraic constraints arises

$$V_z - V_{z-1} = 0 \quad \text{with } z \in [2, N_c]. \tag{4}$$

In total, there are $N_c[5(N_n+N_p)+2N_s-3]-1$ algebraic constraints. Finally, we define the average temperature as

$$T_{\mathrm{bulk}} = \frac{1}{\mathrm{Vol}}\sum_{z=1}^{N_c}\mathrm{Vol}_z T_z \tag{5}$$

where Vol is the total cell volume and Vol_z is the zth subcell volume.

Note that the coupling with the electrochemical part of the model takes place through volumetric heats Q_j and Q_o that depend on several electrochemical algebraic variables, and thus on the electrochemical states.

The following simulations and analysis adopt the cell parameters proposed and experimentally identified in [5], [12], [24] and [25]. In particular, the parameters are representative of the dynamics of 18 650 cells with a graphite anode, a $LiCoO_2$ cathode.[1] Different chemistries will behave similarly, but the main features of the dynamics do not change.

III. Soft-Constrained DUKF Estimator

The UKF is a sigma-point Kalman filter with a particular choice of weighting coefficients (see [26] for the complete details). In the UKF formulation, a set of *sigma-points* is deterministically sampled starting from the previous-step a *posteriori* state estimate and covariance matrix. In the *time-update* step, each of these points is propagated through the system nonlinear state equation; the results are then weighted to generate the current step a *priori* state estimate and covariance matrix. Also, a *priori* sigma-points are passed through the system nonlinear output equation and then weighted to give an estimate of the output and its covariance matrix. Furthermore, the state and output cross-covariance matrix is estimated. Finally, in the *measurement-update* step, the Kalman gain is applied to the difference between the actual and estimated output, in order to compute the current-step a *posteriori* state estimate and covariance matrix. It can be observed that the time-update step of the algorithm is naturally amenable to parallel computing implementation; in fact, each a *priori* sigma-point computation, starting from $\hat{x}^+_{k-1}$ and $P^+_{xx,k-1}$, is completely independent of other sigma-points.

If n_x is the dimension of the state vector, the sigma-points are $2n_x+1$. The covariance matrix $P^+_{xx,0}$ of the initial state estimate is a tuning parameter, which rules the initial dispersion of the sigma-points around the initial state estimate $\hat{x}^+_0$, that is another tuning parameter. The covariance matrix $Q_{\xi\xi}$ of the process disturbance and the covariance matrix R_{vv} of the measurement noise are also important tuning parameters, as well as the other, minor tuning parameters.

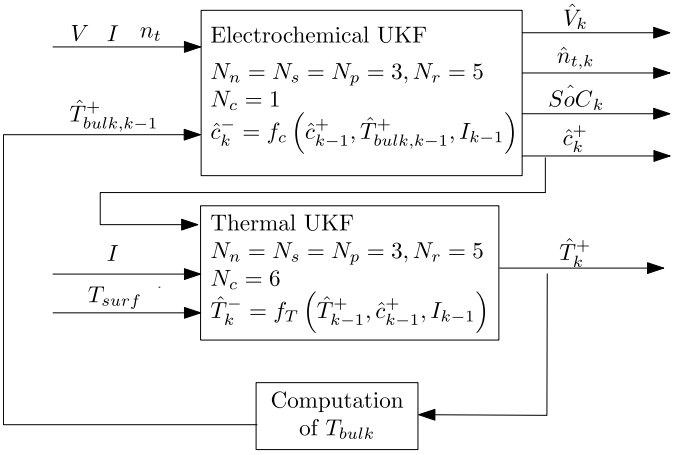

Fig. 2. Scheme of the DUKF estimator. The meaning of the signal n_t is explained in Section III-B.

Applying the UKF structure to the coupled electrochemical–thermal model would lead an intractable problem because of the system dimension. Instead, we propose a dual filter structure to reduce its complexity. The filter exploits the assumption that the electrochemical quantity observation can be carried out assuming a uniform temperature. Fig. 2 represents the resulting structure. The overall observer is composed of two parts: the electrochemical UKF and the thermal UKF. The electrochemical UKF includes only the P2D model of the cell. It receives as inputs the current, the voltage, and the estimated bulk temperature, $\hat{T}_{\mathrm{bulk}}$, which comes from the thermal observer. It provides estimates of all discretized elements of c_s and c_e, and of the SoC. The dimension of the state for the electrochemical part of DUKF is $n_x = (N_r+1)(N_n+N_p)+N_s$. On the

[1]The list of the entire parameters used in the model can be found at https://home.deib.polimi.it/corno/publications.htm

other hand, the thermal UKF includes only the thermal model of the cell and assumes all the N_c subcells to be characterized by the same electrochemical states c_s and c_e (distributed along x and r). It receives as inputs the current and the estimated concentrations vector, which come from the electrochemical part of the observer; it receives the surface temperature as the measured quantity; finally, it provides estimates of the temperatures of all the subcells, gathered in the estimated state vector $\hat{T}$. The dimension of the state for the thermal part of DUKF is $n_x = N_c$. The electrochemical UKF assumes a uniform temperature; the estimation of the electrochemical quantities will be more accurate in the regions whose temperature is closer to the fed one. For this reason, we opted to use the bulk temperature. This leads to an estimation error whose maximum is lower than if we used the core temperature. Using the core temperature would lead to a more accurate estimation of the electrochemical states in the core, but a worse estimation on the surface.

From the computational efficiency standpoint, the proposed structure offers two main advantages:

1) It solves the problem of the parallel configuration for the subcells. Instead of implementing the algebraic constraints (4), as is done in the coupled electrochemical–thermal simulator, the measured quantity V is forced to be the same for all the subcells through the assumption that all the subcells have the same electrochemical state.
2) The monolithic single observer would have an order of $((N_r + 1)(N_n + N_p) + N_s)N_c$ against the order of the DUKF which is $((N_r + 1)(N_n + N_p) + N_s) + N_c$. This comes with a loss of accuracy due to the fact that the electrochemical dynamics is integrated considering the bulk temperature; however, Section IV will show that the loss of accuracy is negligible.

A. Bulter–Volmer Linearization

The UKF is based on the propagation, through the nonlinear dynamics, of $2n_x + 1$ sigma-points at each sampling time; for this particular system, the nonlinear dynamics are characterized by algebraic constraints determined by the Butler–Volmer kinetics (1) in the form of implicit equations. Solving for these constraints is inefficient; in order to speed up the computation, the UKF implementation uses the linearized Butler–Volmer kinetics

$$j_k^{\mathrm{Li}} = \frac{a_s}{R_{\mathrm{ct}}}[\phi_{sk} - \phi_{ek} - U(c_{s(k,N_r)})] \tag{6}$$

where

$$R_{\mathrm{ct}} = \frac{RT}{j_0 F(\alpha_a + \alpha_c)}.$$

B. Soft-Constrained UKF

The straightforward implementation of the DUKF does not lead to satisfactory performance. In many simulations, yet the estimation error of the internal states diverges, when this happens, the total mass of lithium in the model varies. This is of course a nonphysical behavior. Fig. 3 plots the actual and estimated number of moles of Li (n_t) along with the

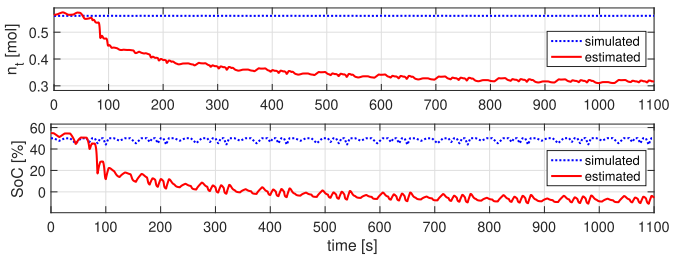

Fig. 3. Number of estimated and simulated moles of lithium during the current pulse cycle (top plot) and estimated bulk SoC (bottom plot).

estimated bulk SoC during a current pulse cycle, designed to keep the SoC around 50%. From the figure, one can see that the estimated SoC diverges, reaching unfeasible values. This happens because the algorithm does conserve the total number of moles of available lithium, or, equivalently, the conservation of total lithium mass. As a matter of fact, although the single sigma-point transformation through the model state equation conserves the total lithium mass, being based on the P2D model formulation, other steps in the UKF algorithm do not provide the same feature. Three steps possibly alter the total lithium mass because of their purely statistical nature: 1) sigma-points computation based on previous step a *posteriori* state estimation and covariance matrix; 2) a *priori* state estimation via weighted sum of sigma-points; and 3) a *posteriori* state estimation via the measurement correction step.

Based on the above considerations, the structure of the electrochemical UKF is amended to avoid divergence in the number of moles of lithium. In the literature, two approaches are present: a *hard-constraint* approach, adding additional algebraic constraints in the sigma-points computation; or a *soft-constraint* approach.

The latter idea consists in modifying the input–output structure of the model by adding a *virtual* measurement, namely the total number of moles of available lithium n_t (constant signal). In this framework, the measured output becomes

$$y = \begin{bmatrix} V \\ n_t \end{bmatrix}$$

where n_t is the total number of moles of lithium in the solid phase (n_s) and in the electrolyte phase (n_e) computed as

$$\begin{aligned} n_s &= \frac{3A}{R_s^3} \int_0^L \int_0^{R_s} \varepsilon_s r^2 c_s \, \mathrm{d}r\mathrm{d}x \\ n_e &= A \int_0^L \varepsilon_e c_e \, \mathrm{d}x. \end{aligned} \tag{7}$$

In this way, we effectively add an additional parameter to the observer. This parameter prevents the drift of the number of lithium moles. Note that n_t is a constant for a given cell at a given aging state and it can be either derived from the identified parameters of the model or can be considered as a tuning parameter of the observer and treated in the same way as R_{vv} or $Q_{\xi\xi}$.

C. Implementation With Parallel Computing

Each sigma-point a *priori* propagation takes place independently of other sigma-points; this structure is thus suitable for

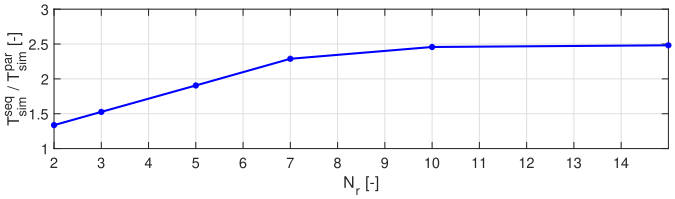

Fig. 4. Ratio between simulation time required by sequential and parallel computing implementation of UKF estimator, for different discretization levels N_r.

parallel computing implementation. Most of the time-update step computational cost can be distributed on multiple cores, so that the time required for this step is ultimately significantly reduced.

The following computational cost analysis quantitatively illustrates this advantage. The dual estimator is run on a sequence of pulses at 10 °C followed by rest periods, both of 10 s duration. Simulations were run in MathWorks MATLAB, with the Parallel Computing Toolbox, on a quad-core machine (2.4 GHz) with 12 GB RAM and solid-state drive. Fig. 4 plots the ratio between the simulation time required by the sequential and parallel implementation, respectively, called $T_{\text{sim}}^{\text{seq}}$ and $T_{\text{sim}}^{\text{par}}$ as a function of N_r, with $N_n = N_s = N_p = 3$ and $N_c = 6$. By observing the figure, it is clear that the estimation algorithm computational burden is reduced by a factor between 1.3 and 2.5 thanks to the parallel implementation.

IV. Validation

This section validates the proposed approach. In the following, we feed the observer data generated using a simulation model. This complete electrochemical–thermal model considers the full set of PDAEs, meaning that it does not decouple the thermal and electrochemical parts, and it does not linearize the Butler–Volmer kinetics. As a result, the order of the simulation model is $((N_r + 1)(N_n + N_p) + N_s)N_c$. The discretization parameters of the simulation model are $N_r = 50$, $N_n = N_p = 5$, $N_s = 3$, and $N_c = 10$, whereas the parameters of the estimation model are $N_r = 5$, $N_n = N_p = N_s = 3$, and $N_c = 6$. See [27] for more details on how the bidirectional coupling is integrated. As a final step, all the measured variables (voltage and surface temperature) are corrupted by zero-mean white noise.

The first step of the validation is the comparison of the simulation model against an experimentally validated CFD model [13]. Fig. 5 plots the comparison between the terminal voltage predicted by our simulator and the output of the CFD model during a phase of the dynamic test shown in Fig. 6. As shown in the figure, the model used in simulation accurately tracks the voltage behavior of a standard validated model.

Armed with this verification, we discuss the performance of the estimation. In what follows, the covariance matrices $P_{xx,c,0}^{+}$, $P_{xx,T,0}^{+}$, $Q_{\xi\xi,c}$, $R_{vv,c}$, and $R_{vv,T}$ are all chosen as diagonal matrices. Recall that $R_{vv,c}$ accounts also for the virtual n_t measurement.

Fig. 7 presents the bulk SoC estimation error (expressed in percentage) during a series of 10 °C current pulses. The

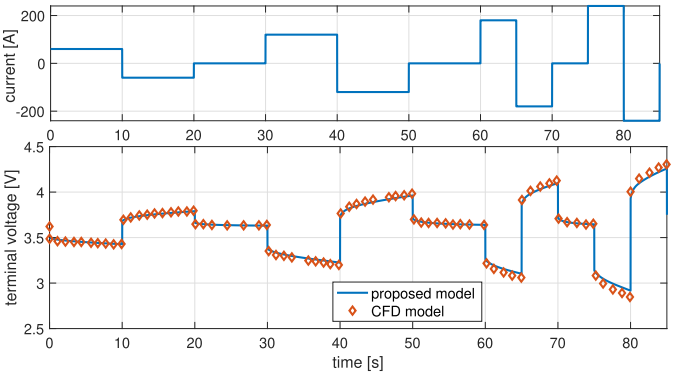

Fig. 5. Voltage response of the model with high rate charge and discharge current profile.

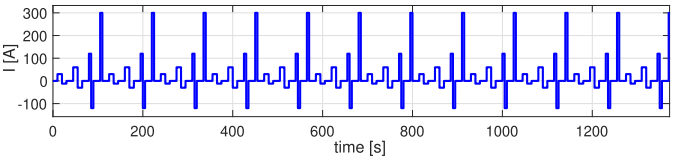

Fig. 6. Current input profile used to validate the DUKF in the dynamic test.

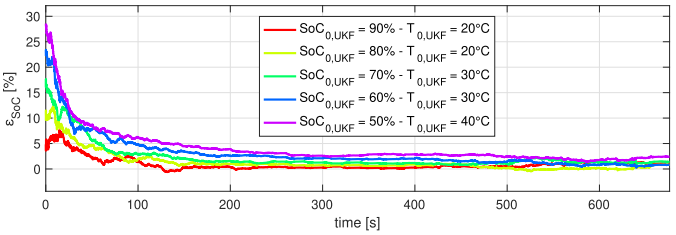

Fig. 7. Bulk SoC estimation results for the current pulses, with several values of $\text{SoC}_{0,\text{UKF}}$ and $T_{0,\text{UKF}}$.

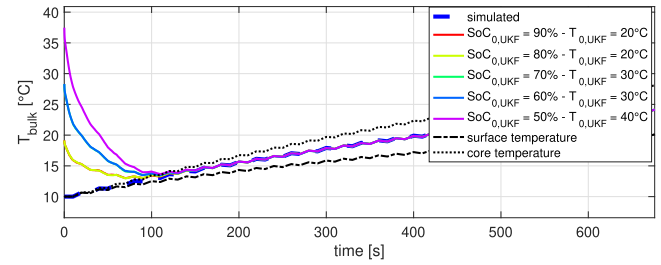

Fig. 8. Bulk temperature estimation results for the current pulses, with several values of $\text{SoC}_{0,\text{UKF}}$ and $T_{0,\text{UKF}}$.

DUKF is initialized at different initial guesses of SoC and T_{bulk}, indicated as $\text{SoC}_{0,\text{UKF}}$ and $T_{0,\text{UKF}}$, respectively. Fig. 8 plots the bulk temperature estimation, comparing it against the real bulk temperature and the core and surface ones. From the figures, one concludes the following.

1) The estimator converges to the true values of SoC and T_{bulk} even for large initialization errors in both the electrochemical and thermal parts, respectively, of up to 50% and up to 30 °C.
2) The initial convergence rate is very fast. For all considered initializations, the SoC error goes below 10% in

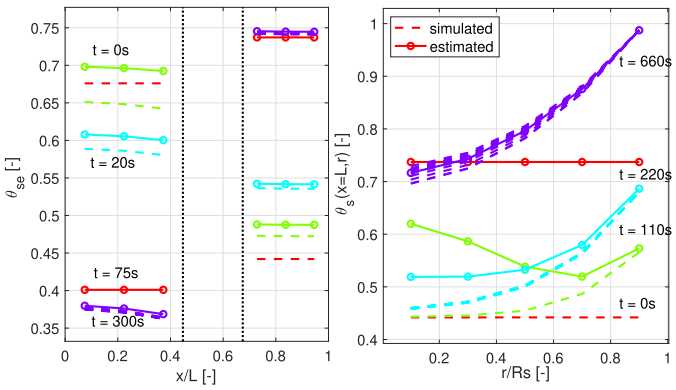

Fig. 9. Surface stoichiometry distribution along the x direction, at different time instants (left). Stoichiometry distribution along the r direction of the spherical particle at $x = L$, at different time instants (right).

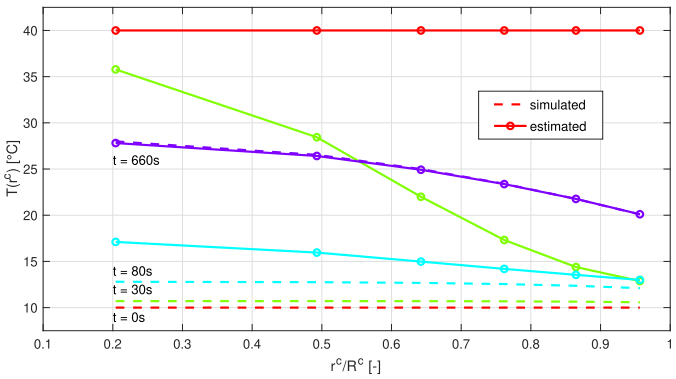

Fig. 10. Temperature distribution along the r^c direction of the cylindrical cell, at different time instants (depicted with different colors) for the current pulses.

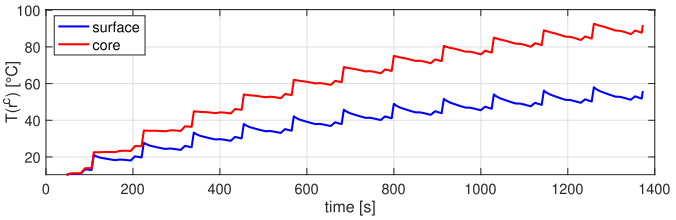

Fig. 11. Simulated temperature profiles at surface and in the core of the cell, under the same current of Fig. 6.

less than 40 s, while the bulk temperature error goes below 5 °C in less than 60 s.

3) After the initial transient (roughly 250 s), the SoC error keeps always under 3% (in the absolute value) and reaches values as low as 1.5% by the end of the test in all cases apart ($\text{SoC}_{0,\text{UKF}} = 50\%$, $T_{0,\text{UKF}} = 40$ °C); the bulk temperature error is always below 0.1 °C (in the absolute value) after the initial transient.

Fig. 9 plots snapshots at different time instants of the estimation of lithium concentration. The left panel plots the estimation of surface stoichiometry along x; the right panel plots the estimation of stoichiometry along the radial direction of a spherical particle close to the positive current collector. The reported simulated results show the electrochemical variables for each of the N_c subcells, each with a different temperature; the DUKF accurately estimates the variables of interest. Note that the surface stoichiometry has a faster convergence than for the center of the active material. This happens because the surface stoichiometry more directly affects the measured voltage. Also, the simulation reaches near-depletion stoichiometry values at the surface (e.g., at $t = 660$ s); in these conditions, the equilibrium potential U exhibits a strong nonlinear dependence on θ_{se}. The DUKF observer is accurate also when this strong nonlinearity is excited. Furthermore, when a consistent temperature gradient along the r_x direction arises (i.e., around $t = 660$ s and to a lesser extent at $t = 220$ s), the different subcells have different stoichiometry distributions along r, in this case, the DUKF estimate sits within the subcell variability, proving that the assumption on which the dual filter structure is based is reasonable.

Finally, Fig. 10 shows the temperature distribution in the cylindrical cell at several time instants. From the figure, the surface temperature converges to the true value in the first seconds of the test, because it is a measured quantity; on the contrary, the convergence of the core temperature requires more time. At the end of the test, a difference of about 7.5 °C is generated between the surface and the core.

A. Remark on Observer Dual Structure

This section further illustrates the advantages and features of the dual structure. The analysis shows that joint temperature and chemical dynamics estimation is required for accurate cell management; at the same time, the analysis exemplifies how the DUKF structure achieves this result with a limited increase in complexity with respect to chemical dynamics only estimators.

Consider the electrochemical UKF subject to the input current of Fig. 6, and initialized with 20% initial SoC error. The simulated temperature profiles from the coupled electrochemical–thermal model are shown in Fig. 11, for the surface and core subcells. Note that the simulator is initialized at $T = 10$ °C. In these conditions, the electrochemical UKF is run with four different temperature inputs: 1) a constant temperature equals to T_{act}, which is equivalent to fix the P2D model parameters to their nominal value; 2) a wrong constant temperature measurement, namely $T = 10$ °C, that is the initial cell temperature in the simulated test; 3) the bulk temperature measurement; and 4) the core temperature measurement. Fig. 12 compares the estimated solid-phase stoichiometry against the stoichiometry of the six subcells that arise from the thermal dynamics discretization. From this analysis, one concludes the following.

1) Lithium concentrations estimation is strongly affected by thermal dynamics. In fact, while surface stoichiometry is estimated with an acceptable accuracy in all considered cases, the stoichiometry at the center of the active material sphere is not correctly estimated by the electrochemical UKF that does not receive *at least* a bulk temperature measurement.
2) Using the bulk or the core temperature as an input to the electrochemical UKF yields similar results. As expected,

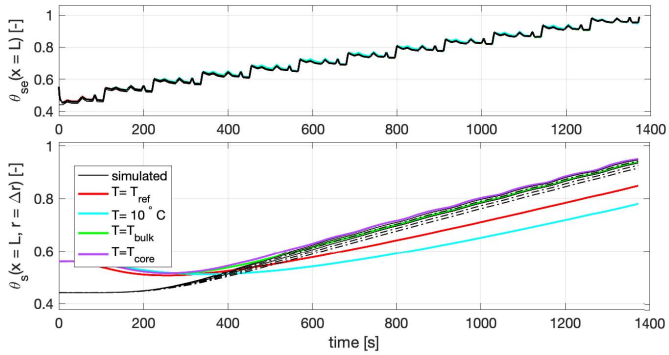

Fig. 12. Solid-phase stoichiometry at surface (top) and active particle core (bottom) of the particle located close to positive electrode current collector for four different estimated temperature profiles.

when using the core temperature, the estimated stoichiometry better tracks the core stoichiometry. The use of the bulk temperature yields an estimation with a lower maximum error considering the six subcells.

These simulations show that the estimation of local temperatures, and in particular of core temperature, is critical for the cell safety and performance. At the end of the test, while the surface temperature (measurable quantity) is still at about 50 °C, the core temperature reaches 95 °C. A simple bulk temperature estimation may not be enough to detect a thermal runaway under demanding input currents.

V. Conclusion

We presented an electrochemical–thermal model-based DUKF observer capable of simultaneously estimate the local temperature and Li concentration in a Li-ion cell. This brief tackles these issues by introducing a soft-constraint that promotes the conservation of mass.

The proposed UKF has several advantages: it does not require a closed-form system; it provides tools for a simple integration of the additional lithium mass conservation constraint; it is amenable to parallel implementation; and it achieves fast and robust convergence from large initial estimation errors.

References

[1] Y. Wang, H. Fang, L. Zhou, and T. Wada, "Revisiting the state-of-charge estimation for lithium-ion batteries: A methodical investigation of the extended Kalman filter approach," *IEEE Control Syst. Mag.*, vol. 37, no. 4, pp. 73–96, Aug. 2017.

[2] K. B. Hatzell, A. Sharma, and H. K. Fathy, "A survey of long-term health modeling, estimation, and control of lithium-ion batteries: Challenges and opportunities," in *Proc. Amer. Control Conf. (ACC)*, Jun. 2012, pp. 584–591.

[3] P. W. C. Northrop, B. Suthar, V. Ramadesigan, S. Santhanagopalan, R. D. Braatz, and V. R. Subramanian, "Efficient simulation and reformulation of lithium-ion battery models for enabling electric transportation," *J. Electrochem. Soc.*, vol. 161, no. 8, pp. E3149–E3157, 2014.

[4] K. A. Smith, C. D. Rahn, and C.-Y. Wang, "Model-based electrochemical estimation and constraint management for pulse operation of lithium ion batteries," *IEEE Trans. Control Syst. Technol.*, vol. 18, no. 3, pp. 654–663, May 2010.

[5] K. Smith and C.-Y. Wang, "Power and thermal characterization of a lithium-ion battery pack for hybrid-electric vehicles," *J. Power Sour.*, vol. 160, no. 1, pp. 662–673, 2006.

[6] C. Forgez, D. Vinh Do, G. Friedrich, M. Morcrette, and C. Delacourt, "Thermal modeling of a cylindrical $LiFePO_4$/graphite lithium-ion battery," *J. Power Sour.*, vol. 195, no. 9, pp. 2961–2968, May 2010.

[7] Q. Wang, P. Ping, X. Zhao, G. Chu, J. Sun, and C. Chen, "Thermal runaway caused fire and explosion of lithium ion battery," *J. Power Sour.*, vol. 208, pp. 210–224, Jun. 2012.

[8] G. L. Plett, "Sigma-point Kalman filtering for battery management systems of LiPB-based HEV battery packs," *J. Power Sour.*, vol. 161, no. 2, pp. 1356–1368, Oct. 2006.

[9] S. J. Moura, F. B. Argomedo, R. Klein, A. Mirtabatabaei, and M. Krstic, "Battery state estimation for a single particle model with electrolyte dynamics," *IEEE Trans. Control Syst. Technol.*, vol. 25, no. 2, pp. 453–468, Mar. 2017.

[10] N. Lotfi, R. G. Landers, J. Li, and J. Park, "Reduced-order electrochemical model-based SOC observer with output model uncertainty estimation," *IEEE Trans. Control Syst. Technol.*, vol. 25, no. 4, pp. 1217–1230, Jul. 2017.

[11] M. Doyle, "Modeling of galvanostatic charge and discharge of the lithium/polymer/insertion cell," *J. Electrochem. Soc.*, vol. 140, no. 6, pp. 1526–1533, 1993.

[12] K. Smith and C.-Y. Wang, "Solid-state diffusion limitations on pulse operation of a lithium ion cell for hybrid electric vehicles," *J. Power Sour.*, vol. 161, no. 1, pp. 628–639, Oct. 2006.

[13] K. A. Smith, C. D. Rahn, and C.-Y. Wang, "Control oriented 1D electrochemical model of lithium ion battery," *Energy Convers. Manage.*, vol. 48, no. 9, pp. 2565–2578, Sep. 2007.

[14] N. A. Chaturvedi, R. Klein, J. Christensen, J. Ahmed, and A. Kojic, "Algorithms for advanced battery-management systems," *IEEE Control Syst. Mag.*, vol. 30, no. 3, pp. 49–68, Jun. 2010.

[15] A. M. Bizeray, S. Zhao, S. R. Duncan, and D. A. Howey, "Lithium-ion battery thermal-electrochemical model-based state estimation using orthogonal collocation and a modified extended Kalman filter," *J. Power Sour.*, vol. 296, pp. 400–412, Nov. 2015.

[16] M. Corno, N. Bhatt, S. M. Savaresi, and M. Verhaegen, "Electrochemical model-based state of charge estimation for Li-ion cells," *IEEE Trans. Control Syst. Technol.*, vol. 23, no. 1, pp. 117–127, Jan. 2015.

[17] S. Marelli and M. Corno, "A soft-constrained unscented Kalman filter estimator for Li-ion cells electrochemical model," in *Proc. IEEE 56th Annu. Conf. Decis. Control (CDC)*, Dec. 2017, pp. 1535–1540.

[18] A. Stegmeier *et al.*, "Evaluation of fine-grained parallelism in AUTOSAR applications," in *Proc. Int. Conf. Embedded Comput. Syst., Archit., Modeling Simulation (SAMOS)*, Jul. 2017, pp. 121–128.

[19] N. Lotfi, J. Li, R. G. Landers, and J. Park, "Li-ion battery state of health estimation based on an improved single particle model," in *Proc. Amer. Control Conf. (ACC)*, May 2017, pp. 86–91.

[20] L. O. Valøen and J. N. Reimers, "Transport properties of LiPF6-based Li-ion battery electrolytes," *J. Electrochem. Soc.*, vol. 152, no. 5, pp. A882–A891, 2005.

[21] S. Al Hallaj, H. Maleki, J. S. Hong, and J. R. Selman, "Thermal modeling and design considerations of lithium-ion batteries," *J. Power Sour.*, vol. 83, nos. 1–2, pp. 1–8, Oct. 1999.

[22] T. I. Evans, "A thermal analysis of a spirally wound battery using a simple mathematical model," *J. Electrochem. Soc.*, vol. 136, no. 8, pp. 2145–2152, 1989.

[23] S. Anwar, C. Zou, and C. Manzie, "Distributed thermal-electrochemical modeling of a lithium-ion battery to study the effect of high charging rates," *IFAC Proc. Volumes*, vol. 47, no. 3, pp. 6258–6263, 2014.

[24] Y. Kim, J. B. Siegel, and A. G. Stefanopoulou, "A computationally efficient thermal model of cylindrical battery cells for the estimation of radially distributed temperatures," in *Proc. Amer. Control Conf.*, Jun. 2013, pp. 698–703.

[25] J. B. Sangiri, S. Ghosh, and C. Chakraborty, "Electro-thermal modeling of lithium-ion cell for higher discharge rate applications," in *Proc. 21st Century Energy Needs-Mater., Syst. Appl. (ICTFCEN)*, Nov. 2016, pp. 1–6.

[26] S. J. Julier, J. K. Uhlmann, and H. F. Durrant-Whyte, "A new approach for filtering nonlinear systems," in *Proc. Amer. Control Conf. (ACC)*, 1995, pp. 1628–1632.

[27] L. Onesto, S. Marelli, and M. Corno, "Control-oriented coupled electrochemical thermal model for Li-ion batteries," in *Proc. IEEE 56th Annu. Conf. Decis. Control (CDC)*, Dec. 2017, pp. 5026–5031.